Improved performance of planar perovskite solar cells via ethanol-vapor annealing treatment

J. WU, J. J. DONG[*], H. Y. HAO, J. XING, H. LIU
School of Science, China University of Geosciences (Beijing), 29 Xue Yuan Road, Haidian District, Beijing, 100083, China

In this paper, ethanol-vapor annealing treatment on perovskite thin films is reported, aiming to increase grain size, reduce defect states and improve crystallinity of the perovskite films, thus improving the performance of the planar perovskite solar cells (PSCs). Here, we show a two-step annealing method, ethanol-vapor annealing followed by normal heat treatment in Ar atmosphere, to prepare pinhole-free perovskite films with large grain size and few defects. The planar PSCs containing perovskite films prepared by this two-step annealing, exhibit much higher power conversion efficiency, which has been improved from 9.62% to 12.00%. Thus, our method provides a facile and simple way to improve the device performance of PSCs.

1. Introduction

Organic-inorganic halide perovskite based solar cells have attracted great attention in recent years, due to their high optical absorption coefficient, long carrier diffusion length, high carrier mobility, and low material cost [1-4]. The power conversion efficiency (PCE) of the planar perovskite solar cells (PSCs) has taken a tremendous step forward, from 3.9% in 2009 to a recently reported 22.1% [5-7], approaching the monocrystalline silicon solar cells. Up to now, the huge leap forward has been made in stability, interface engineering, transport characteristics, morphology, hysteresis, and interrelated physical and chemical mechanisms [8-17]. The perovskite active layer in PSCs can be easily prepared by low-cost solution process, the one-step method, two-step method and variations thereof [18-19]. In the one-step method, a mixed perovskite precursor solution with PbX_2 and MAX (MA: CH_3NH_3) (X= Cl, Br, or I) in a polar solvent is spin-coated onto the substrate and annealed on the hot plate. Although easy to operate, it is difficult to control the growth process and final morphology of perovskite films, because the evaporation of solvent and crystallization of perovskite films take place simultaneously during the spin-coating and annealing process [20]. To address this issue, the two-step sequential deposition method is proposed, which entails dip-coating or spin-coating PbX_2 and MAX solution separately, followed by heat-treatment at 70-150°C. As the evaporation of solvent and crystallization of perovskite films occurs asynchronously, it is much easier to control the growth process as well as final

morphology of perovskite films, compared with the one-step method. However, the crystallization of perovskite films prepared by the two-step method is usually incomplete, in other words, there is usually too much residue PbI_2 in the perovskite films, which will decrease the performance of PSCs [21]. To address this problem, huge efforts, such as solvent engineering [22], gas-blowing [23], or solvent-vapor annealing [24], have been employed to improve further the quality of the perovskite films. Among them, solvent-vapor annealing was demonstrated most manageable and effective to increase the crystallinity of perovskite films [25-26].

In this work, we introduce ethanol-vapor annealing treatment to increase the crystallinity and grain size of the perovskite films on the compact TiO_2 layer. As MAI rather than PbI_2 possess a good solubility in ethanol, the ethanol-vapor selectively controls the dynamic transitions of MAI, leaving the PbI_2 dense layer to ensure a pinhole-free perovskite layer. By introducing the ethanol-vapor in the thermal annealing treatment, MAI can easily diffuse into the PbI_2 film via dissolving in the ethanol-vapor, due to its good solubility. Besides, the ethanol-vapor can diffuse into the grain boundary and promote the growth of the grains. After the ethanol-vapor annealing treatment, a normal heat treatment in Ar atmosphere in the glove box is also essential to drive out the excess organic solvent and ethanol-vapor adsorbed on the surface of the perovskite film, as well as promote reaction of MAI and PbI_2 completely. This two-step annealing (ethanol-vapor annealing and normal heat treatment) dramatically improved the electronic properties

of the perovskite layer. And the planar – heterojunction -structured PSCs, with the active layers prepared by the two-step annealing treatment, exhibit a maximum PCE of 12.00%, which is improved by ~25% compared with the PSCs prepared by the normal two-step method without ethanol-vapor annealing.

2. Experimental procedure

2.1. Fabrication of perovskite solar cells

A planar device structure was adopted for the device fabrication, as shown in Fig. 1. There, the perovskite films were fabricated by the two-step spin-coating method. Fluorine-doped transparent conducting SnO_2-coated glass substrates (FTO) with a sheet resistance of 7Ωsq-1 were cleaned with acetone, ethanol, isopropanol, deionized water and isopropanol respectively. A TiO_2 compact electron transport layer was then coated on the FTO substrates by spin coating at 3000 rpm for 30 s (repeat four times, followed by annealing at 150°C for 5 min for each time), and the film was annealed at 500°C for 30 min in air. After that, the perovskite layer was deposited by the two-step spin-coating method.
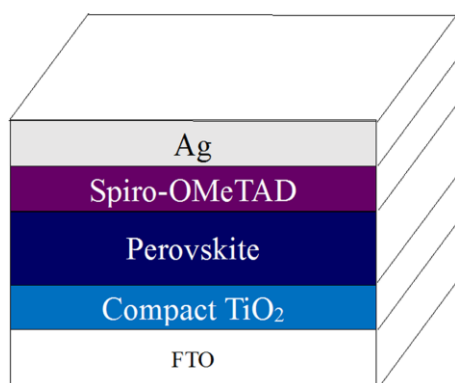
Fig. 1. A schematic structure of the planar PSCs

Fig. 2 presents the two-step sequential deposition process with ethanol-vapor annealing. As shown in Fig. 2, first, 1M of PbI_2 in N,N-dimethylformamide (DMF) was spin coated onto the electron transport layer at 3000 rpm for 30 s, then annealed at 70°C for 15 min; second, after the PbI_2 films had cooled down to room temperature, the solution of MAI (60 mg in 1mL isopropanol) was spin coated onto PbI_2 at 4000 rpm for 45 s; third, the as-grown $MAPbI_3$ films were divided into three groups for different heat treatment. Films of Group 1 were annealed at 110°C for 30 min in Ar atmosphere; films of Group 2 were annealed at 110°C for 5 min in the ethanol-vapor, and then annealed at 110°C for 15 min in Ar atmosphere immediately; films of Group 3 were annealed at 110°C for 15 min in the ethanol-vapor, and then annealed at 110°C for 15 min in Ar atmosphere immediately. The preparation

of the TiO_2 compact layer, $MAPbI_3$ films and the heat treatment of the three groups were carried out in a Ar-filled glove box (< 0.1PPM O_2 and H_2O). After the heat treatment, the films were taken out from the glove box for 2,2′,7,7′-Tetrakis[N,N-di(4-methoxyphenyl)amino]-9,9′-spiro-bifluorene (Spiro-OMeTAD) hole transport layer (HTL) coating. The Spiro-OMeTAD solution was spin-coated at 2000 rpm for 45 s in ambient air, where 80 mg Spiro-OMeTAD in 1 mL chlorobenzene solution was employed with the addition of 28.8 μL 4-tert-butylpyridine (TBP) and 17.7 μL lithium bis(trifluoro-methanesulfonyl)imide (Li-TFSI) solution (520mg Li-TFSI in 1mL acetonitrile). Finally, a Ag back electrode was deposited by thermal evaporation at a pressure of 3.8 × 10^{-6} torr. The effective area of the solar cell is 0.1 cm^2.
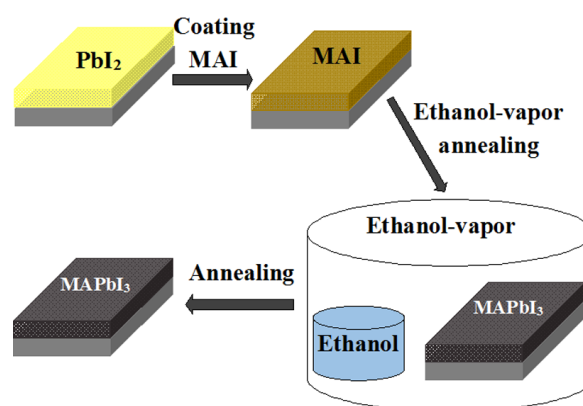
Fig. 2. Schematic illustration of the two-step sequential deposition process with ethanol-vapor treatment

2.2. Characterization

Current density-voltage (J-V) characteristic curves of photovoltaic cells were measured by a source meter (Keithley, 2400) with a solar simulator (Zolixss150) under 100 mW·cm^{-2} AM 1.5G illumination, the light intensity was calibrated by means of a silicon reference solar cell, The area of the devices were 0.1 cm^2. Typical J-V curves were obtained from scanning in reverse bias direction at the step width of 200 mV. The voltage was scanned from 1.2 V to -0.2 V at a rate of 100 mV·s^{-1}. The J-V measurement was carried out in ambient air. An emission Hitachi S-4800 was used to obtain Scanning Electron Microscopy (SEM) images with the electron beam acceleration in the range of 15 KV to 50 KV. The characteristic X-ray diffraction (XRD) patterns were recorded between 10° to 60°, using the Cu-Kα radiation at 1.5405 Å. The light absorbance spectra were required using a Cary 5000 UV-vis spectrophotometer in the wavelength range of 200 nm to 1200 nm with 1 nm increment. The wavelength of exciting light was 510 nm in the Steady-state Photoluminescence (PL) (Fluoromax -4C-L) measurements, and the Time-resolved PL (F900)

measurements was 450 nm. All the measurements of the three groups of films were carried out in ambient air without humidity control.

3. Results and discussions

The crystallinity of as-grown MAPbI$_3$ films was characterized by the XRD. Fig. 3 shows the XRD patterns of the three groups of MAPbI$_3$ films prepared by normal thermal annealing and ethanol-vapor annealing for different time, as described in the experimental part. It can be seen that the three groups of MAPbI$_3$ films exhibit almost the same crystalline phase. The diffraction peaks were observed at 2θ values of 14.06°, 20.00°, 23.45°, 28.42°, 31.86°, 40.59°, 43.21° and 50.21° correspond to the reflection planes of (110), (112), (202), (220), (310), (224), (314) and (404) of the tetragonal perovskite structure [27], respectively. It is also observed that the characteristic peak of PbI$_2$ is present at 12.69° from the XRD patterns of the three groups, implying there is a little bit of PbI$_2$ residual for all of the three groups of MAPbI$_3$ films. It is reported that a little bit of PbI$_2$ can improve the performance of PSCs by passivating the defects in the perovskite films [28]. Besides, the intensity of the PbI$_2$ peak at 12.69° from the XRD patterns of the three groups is nearly the same, demonstrating there is little difference in the amount of

PbI$_2$ residual for the three groups of MAPbI$_3$ films. So, the ethanol-vapor annealing process did not change the composition and crystallinity of the perovskite films.
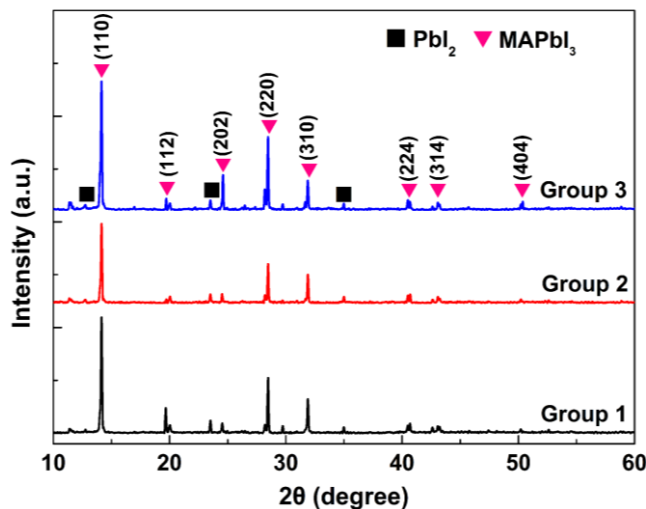
Fig. 3. XRD spectra of perovskite films on quartz substrates prepared by normal thermal annealing (Group 1), ethanol-vapor annealing for 5 min (Group 2) and 15 min (Group 3), as described in the experimental part
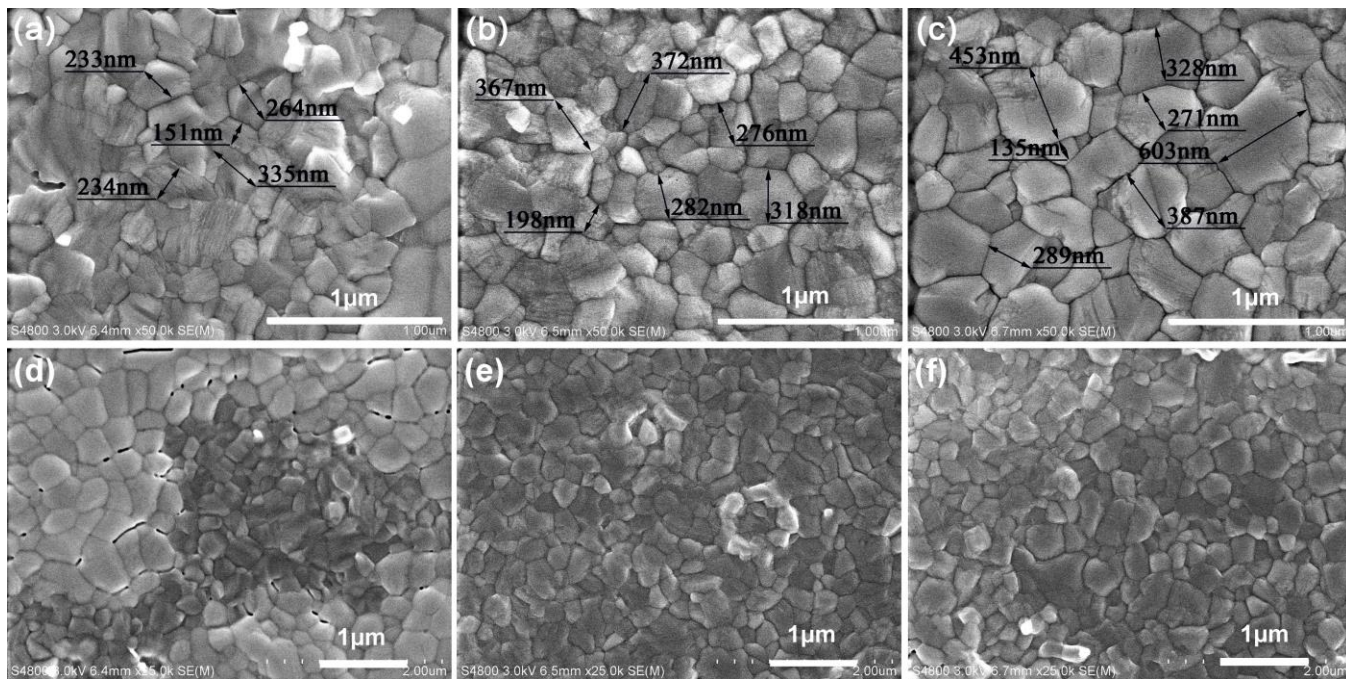
Fig. 4. SEM surface images of the three groups of perovskite films on the compact-TiO$_2$ layer: (a), (d) reference sample without ethanol-vapor annealing process (Group 1); (b), (e) ethanol-vapor annealing for 5 min (Group 2); (c), (f) ethanol-vapor annealing for 15 min (Group 3)

Fig. 4a-f shows the SEM surface images of perovskite films prepared by normal thermal annealing and ethanol-vapor annealing for different time on the compact-TiO$_2$ layer. It can be seen that the morphology of the perovskite films was very sensitive to the ethanol-vapor annealing. The perovskite film without

ethanol-vapor annealing (Fig. 4a, d) exhibits inhomogeneous and small grain size along with amount of pinholes, which have been demonstrated to be the primary reason for poor repeatability and photoelectric properties of PSCs. On the contrary, much more excellent perovskite films (Fig. 4b, c, e, and f) are obtained after introducing ethanol-vapor annealing process, such as enhanced grain size, and greatly reduced pinholes. The high-resolution SEM images (Fig. 4a-c) reveal that the average grain size of perovskite films prepared by normal thermal annealing and ethanol-vapor annealing for 5 min and 15 min are 250 nm, 300 nm and 350 nm, respectively, indicating the grain size of perovskite films increases with the time of ethanol-vapor annealing. However, ethanol-vapor annealing for too long time may induce the decomposition of the $MAPbI_3$ crystals.

UV-vis absorption spectrum of $MAPbI_3$ films are presented in Fig. 5. All the three perovskite films show an absorbance at a threshold of about 780 nm in the overall visible region, which conforms to the reported results, which indicates the formation of $MAPbI_3$ crystallites [29]. The perovskite film without ethanol-vapor annealing (Group 1) shows lowest absorption among all the three samples, which is attributed to the smaller perovskite crystallites compared with the films with ethanol-vapor annealing. The maximum absorbance observed for the sample prepared by ethanol-vapor annealing for 5 min (Group 2) is attributed to the larger crystallite size and better grain interconnections as shown in the SEM images. The perovskite film prepared by ethanol-vapor annealing for 15 min (Group 3) presents a decrease in absorbance due to the onset of dissociation of $MAPbI_3$ [27]. The weak absorption shoulder at about 510 nm, which appears in all the three spectra as shown in Fig. 5, is a characteristic feature of PbI_2 [30], implying the residual of PbI_2 as confirmed by the XRD measurement.
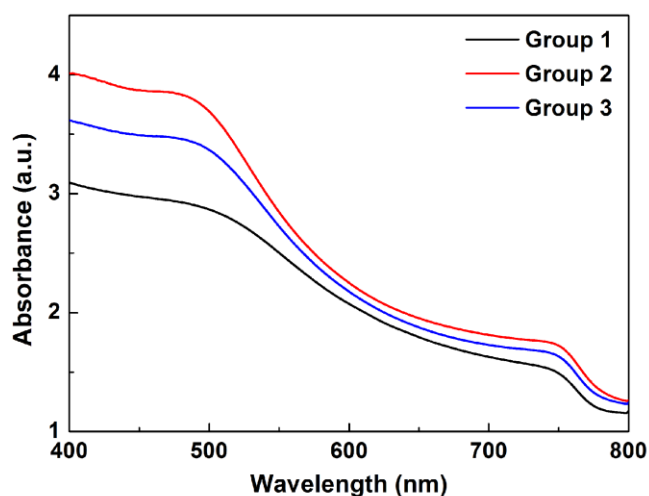
To further investigate the influence of ethanol-vapor annealing process on charge transport properties between TiO_2 and perovskite layer, steady-state and time-resolved PL spectra of the perovskite films on FTO/compact-TiO_2 substrates are measured. Fig. 6a shows the steady-state PL spectra of perovskite films on FTO/compact-TiO_2 substrates with and without ethanol-vapor annealing. Here, the excitation wavelength in this measurement is 510 nm, and the Characteristic emission peaks appear in about 775 nm, which is consistent with other groups' results [31]. As can be seen, the perovskite film prepared by normal thermal annealing (Group 1) shows the strongest PL peak, which is quenched for the samples prepared by ethanol-vapor annealing (Group 2 and 3). The perovskite film prepared by ethanol-vapor annealing for 5 min (Group 2) has the lowest peak intensity, indicating that the ethanol-vapor annealing could reduce the defect states and improve the crystallinity of the perovskite films, and then accelerate electron extraction from the perovskite films to the compact-TiO_2 layers. However, long-time ethanol-vapor annealing, such as 15 min, will lead to the dissociation of $MAPbI_3$. More efficient carrier transport achieved by the ethanol-vapor annealing process maybe a contribution to the enhancement in the photovoltaic efficiency.

The time-resolved PL spectra can confirm the faster electron extraction process of perovskite films prepared by ethanol-vapor annealing, so we further measured the time-resolved PL spectra. Fig. 6b shows the PL decay curves monitored at the wavelength of 775nm, extracted from the perovskite films prepared with and without ethanol-vapor annealing process on the FTO/compact-TiO_2 substrates. The corresponding lifetimes of the perovskite films are acquired by fitting the dates with bi-exponential decay function [32]. The life time is 8.25 ns for the perovskite film prepared without ethanol-vapor annealing process (Group 1), which is reduced when introducing ethanol-vapor annealing process, The lifetimes of the perovskite films prepared by ethanol-vapor annealing for 5 min and 15 min are 7.46 ns and 7.64 ns respectively, indicating the faster electron extraction process compared with the perovskite film without ethanol-vapor annealing. The faster electron extraction process after ethanol-vapor annealing is due to the reduced defect states and improved crystallinity of the perovskite films, as confirmed by the steady-state PL spectra. Therefore, introducing the ethanol-vapor annealing process can reduce the defect states, improve the crystallinity, and thus promote charge transport between TiO_2 and the perovskite layer.

Fig. 5. UV-vis absorption spectrum of MAPbI$_3$ films on quartz substrates without ethanol-vapor annealing process (Group 1), ethanol-vapor annealing for 5 min (Group 2) and 15 min (Group 3)
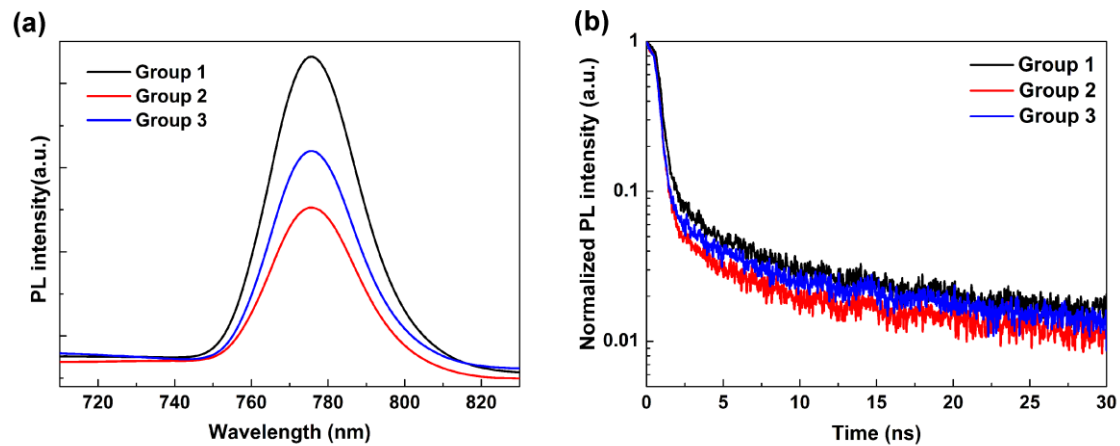
Fig. 6. Charge transport properties between TiO2 and perovskite layer: (a) steady-state PL spectra and (b) time-resolved PL decays of perovskite films prepared by normal thermal annealing (Group 1), ethanol-vapor annealing for 5 min (Group 2) and 15 min (Group 3)

Table 1. Device performance parameters of the PSCs fabricated with films in group 1, 2 and 3

Perovskite layer	J_{SC} (mA/cm^2)	V_{OC} (V)	FF(%)	PCE(%)
Group 1	19.70	0.865	56.45	9.62
Group 2	21.22	0.984	57.47	12.00
Group 3	20.07	0.923	60.30	11.17

A device structure of FTO/Compct-TiO$_2$/MAPbI$_3$/Spiro-OMeTAD/Ag is applied for PSCs. During the fabrication process, 4 solar cells were fabricated in each FTO substrate. Among which, if the maximum photon conversion efficiency deviation is less than 3% in at least 3 solar cells with higher PCE values, then their performance parameters will be recorded. The highest PCE values in the records were adopted here for comparison. There, 5 samples were made for each example, among which, the PCE and other key parameters deviation for each example is less than 3%, thus the results are believable [33]. Fig. 7a shows the cross-section SEM image of the device with the structure FTO/Compct-TiO$_2$/MAPbI$_3$/Spiro-OMeTAD /Ag. The ~50 nm compact TiO$_2$ layer acts as the electron-accepting or hole-blocking layer, the ~300 nm perovskite film functions as the active optical absorption layer, and the ~150 nm Spiro-OMeTAD film served as the hole-collecting layer. FTO glass and the ~150 nm Ag layer were used as the charge-collecting electrodes [20]. Fig. 7b

shows the J-V characteristics of the devices fabricated with perovskite films in group 1, 2 and 3 under AM 1.5G one sun (100 mW·cm^{-2}) illumination, and the corresponding parameters, including open-circuit voltage (V_{OC}), short-circuit current (J_{SC}), fill factor (FF) and PCE are listed in Table 1. The best-performing reference device containing perovskite films prepared without ethanol-vapor annealing (Group 1) showed PCE of 9.62%, with J_{SC} of 19.70 mA/cm^2, V_{OC} of 0.865 V, and FF of 56.45%. When introducing ethanol-vapor annealing, the devices showed significant improvements in all of the photovoltaic parameters. There into, the device containing perovskite films prepared with ethanol-vapor annealing for 5 min (Group 2) gave the highest PCE of 12.00%, with J_{SC} of 21.22 mA/cm^2, V_{OC} of 0.984 V, and FF of 57.47%, which was attributed to the increased grain size, reduced defect states and improved crystallinity of the perovskite films as mentioned earlier. However, slightly hysteresis phenomena can be observed from the J-V curve and the FF is only around 60%. We shall eliminate this situation and further improve the FF by interface modification in future, which is identified as an efficient approach for significantly promoting electron injection, enhancing electron transfer and reducing the charge recombination. Fig. 8 shows the IPCE spectrum and integrated current of the best performing PSC fabricated with the perovskite film prepared by ethanol-vapor annealing for 5 min (Group 2). The integral J_{SC} calculated from the IPCE for the best performing PSC is 20.17 mA/cm^2, which is close to the measured J_{SC} shown in Table 1.
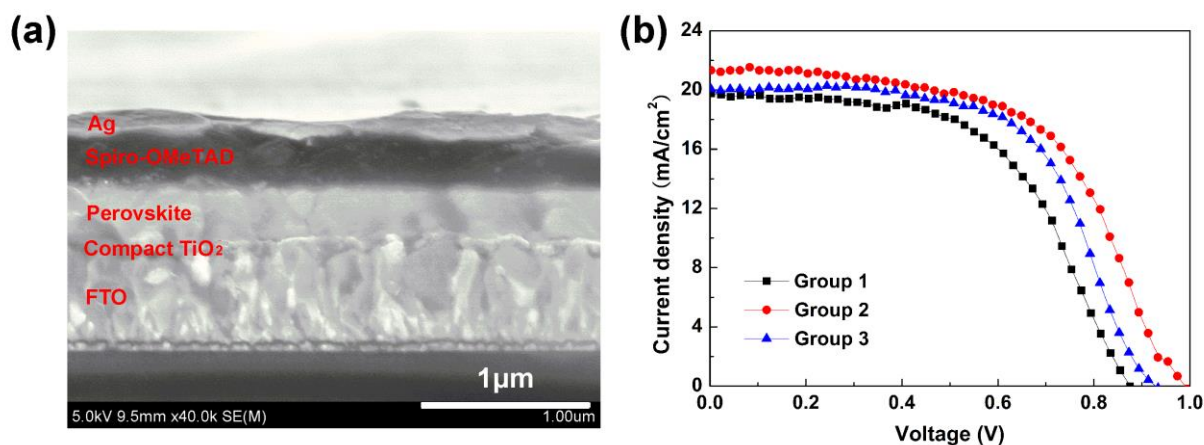
Fig. 7. (a) Cross-section SEM image of the device, with the structure FTO/Compct-TiO$_2$/MAPbI$_3$/Spiro-OMeTAD/Ag; (b) J-V characteristics of the PSCs fabricated with films in group 1, 2 and 3 under AM 1.5G one sun (100 mW·cm^{-2}) illumination
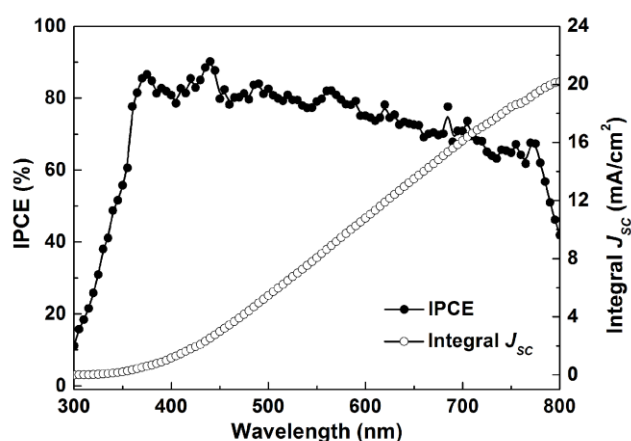
Fig. 8. The IPCE spectrum and integrated current of the best performing PSC fabricated with the perovskite film prepared by ethanol-vapor annealing for 5 min (Group 2)

4. Conclusions

In conclusion, we performed ethanol-vapor annealing process on the perovskite films, in order to increase grain size, reduce defect states and improve crystallinity of the perovskite films, and thus boost the performance of the planar PSCs. XRD, SEM and UV-visible absorption measurements were carried out to confirm the role of ethanol-vapor annealing in increasing grain size and improving crystallinity of the perovskite films. Steady-state and time-resolved PL spectra proved that the charge transport between TiO$_2$ and the perovskite layer was promoted by virtue of ethanol-vapor annealing. As a result, the efficiency of the planar PSCs was increased great from 9.6% to 12%. Our method provides a new route to improve the performance of PSCs.

References

[1] Y. Ogomi, A. Morita, S. Tsukamoto, T. Saitho, N. Fujikawa, Q. Shen, T. Toyoda, K. Yoshino, S. S. Pandey, T. Ma, S. Hayase, J. Phys. Chem. Lett. **5**, 1004 (2014).

[2] S. D. Stranks, G. E. Eperon, G. Grancini, C. Menelaou, M. J. P. Alcocer, T. Leijtens, L. M. Herz, A. Petrozza, H. J. Snaith, Science **342**, 341 (2013).

[3] Y. F. Wang, J. Wu, P. Zhang, D. Liu, T. Zhang, L. Ji, X. L. Gu, Z. D. Chen, S. B. Li, Nano Energy **39**, 616 (2017).

[4] N. G. Park, M. Grätzel, T. Miyasaka, K. Zhu, K. Emery, Nature Energy **1**, 16152 (2016).

[5] P. Zhang, J. Wu, T. Zhang, Y. F. Wang, D. T. Liu, H. Chen, L. Ji, C. H. Liu, W. Ahmad, Z. D. Chen, S. B. Li, Adv. Mater. 1703737 (2017).

[6] D. Bi, W. Tress, M. I. Dar, G. Peng, J. Luo, C. Renevier, K. Schenk, A. Abate, F. Giordano, J. P. C. Baena, J. D. Decoppet, S. M. Zakeeruddin, M. K. Nazeeruddin, M. Grätzel, A. Hagfeldt, Science Advances **2**, 1501170 (2016).

[7] P. Zhang, J. Wu, Y. F. Wang, H. Sarvari, D. T. Liu, Z. D. Chen, S. B. Li, J. Mater. Chem. A **5**, 17368 (2017).

[8] J. You, L. Meng, T. B. Song, T. F. Guo, Y. M. Yang, W. H. Chang, Z. Hong, H. Chen, H. Zhou, Q. Chen, Y. Liu, N. De Marco, Y. Yang, Nat. Nanotechnol. **11**, 75 (2016).

[9] H. Tan, A. Jain, O. Voznyy, X. Lan, F. P. G. Arquer, J.

Z. Fan, Q. B. Rafael, M. Yuan, B. Zhang, Y. Zhao, F. Fan, P. Li, L. N. Quan, S. Hoogland, E. H. Sargent, Science **355**, 722 (2017).

[10] Y. Xu, T. Liu, Z. Li, B. Feng, S. Li, J. Duan, C. Ye, J. Zhang, H. Wang, Applied Surface Science **388**, 89 (2016).

[11] H. Zhou, Q. Chen, G. Li, S. Luo, T. B. Song, H. S. Duan, Z. Hong, J. You, Y. Liu, Y. Yang, Science **345**, 542 (2014).

[12] T. M. Brenner, D. A. Egger, L. Kronik, G. Hodes, D. Cahen, Nature Reviews Materials **1**, 15007 (2016).

[13] B. J. P. Correa, M. Anaya, G. Lozano, W. Tress, K. Domanski, M. Saliba, T. Matsui, T. J. Jacobsson, M. E. Calvo, A. Abate, M. Gratzel, H. Miguez, A. Hagfeldt, Adv. Mater. **28**, 5031 (2016).

[14] W. Ke, C. Xiao, C. Wang, B. Saparov, H. S. Duan, D. Zhao, Z. Xiao, P. Schulz, S. P. Harvey, W. Liao, W. Meng, Y. Yu, A. J. Cimaroli, C. S. Jiang, K. Zhu, M. Al-Jassim, G. Fang, D. B. Mitzi, Y. Yan, Adv. Mater. **28**, 5214 (2016).

[15] A. Giuri, S. Masi, S. Colella, A. Kovtun, S. Dell'Elce, E. Treossi, A. Liscio, C. Esposito Corcione, A. Rizzo, A. Listorti, Advanced Functional Materials **26**, 6985 (2016).

[16] Y. Yuan, Q. Wang, Y. Shao, H. Lu, T. Li, A. Gruverman, J. Huang, Advanced Energy Materials **6**, 1501803 (2016).

[17] Y. Liu, Z. Hong, Q. Chen, H. Chen, W. H. Chang, Y. M. Yang, T. B. Song, Y. Yang. Adv. Mater. **28**, 440 (2016).

[18] Y. Zhou, M. Yang, W. Wu, A. L. Vasiliev, K. Zhu, N. P. Padture, Journal of Materials Chemistry A **3**, 8178 (2015).

[19] Q. Jiang, L. Zhang, H. Wang, X. Yang, J. Meng, H. Liu, Z. Yin, J. Wu, X. Zhang, J. You, Nature Energy **2**, 16177 (2016).

[20] M. Lv, X. Dong, X. Fang, B. Lin, S. Zhang, J. Ding, N. Yuan, RSC Advances **5**, 20521 (2015).

[21] Y. Xie, F. Shao, Y. Wang, T. Xu, D. Wang, F. Huang, ACS Appl Mater Interfaces **7**, 12937 (2015).

[22] N. J. Jeon, J. H. Noh, Y. C. Kim, W. S. Yang, S. Ryu, S. I. Seok, Nat. Mater. **13**, 897 (2014).

[23] F. Huang, Y. Dkhissi, W. Huang, M. Xiao, I. Benesperi, S. Rubanov, Y. Zhu, X. Lin, L. Jiang, Y. Zhou, A. Gray-Weale, J. Etheridge, C. R. McNeill, R. A. Caruso, U. Bach, L. Spiccia, Y. B. Cheng, Nano Energy **10**, 10 (2014).

[24] C. Liu, K. Wang, C. Yi, X. Shi, A. W. Smith, X. Gong, A. J. Heeger, Advanced Functional Materials **26**, 101 (2016).

[25] Z. Xiao, Q. Dong, C. Bi, Y. Shao, Y. Yuan, J. Huang, Adv. Mater. **26**, 6503 (2014).

[26] Y. F. Wang, S. B. Li, P. Zhang, D. T. Liu, X. L. Gu, H. Sarvari, Z. B. Ye, J. Wu, Z. M. Wang, Z. D. Chen, Nanoscale **8**, 19654 (2016).

[27] B. Tripathi, P. Bhatt, K. P. Chandra, P. Yadav, B. Desai, P. M. Kumar, M. Kumar, Solar Energy Materials and Solar Cells **132**, 615 (2015).

[28] Y. C. Kim, N. J. Jeon, J. H. Noh, W. S. Yang, J. Seo, J. S. Yun, A. Ho-Baillie, S. Huang, M. A. Green, J. Seidel, T. K. Ahn, S. I. Seok, Advanced Energy Materials **6**, 1502104 (2016).

[29] Y. Guo, C. Liu, H. Tanaka, E. Nakamura, J. Phys. Chem. Lett. **6**, 535 (2015).

[30] J. Tauc, R. Grigorovici, A. Vancu, Phys Status Solidi B **15**, 627 (1966).

[31] A. R. Pascoe, S. Meyer, W. Huang, W. Li, I. Benesperi, N. W. Duffy, L. Spiccia, U. Bach, Y. B. Cheng, Advanced Functional Materials **26**, 1278 (2016).

[32] J. J. Zhao, P. Wang, Z. H. Liu, L. Y. Wei, Z. Yang, H. R. Chen, X. Q. Fang, X. L. Liu, Y. H. Mai, Dalton Transactions **44**, 17841 (2015).

[33] J. J. Dong, J. Wu, H. Y. Hao, J. Xing, H. Liu, H. Gao, Nanoscale Res. Lett. **12**, 529 (2017).

_____
*Corresponding author: jjdong@semi.ac.cn